6th European Conference on Computational Mechanics (ECCM 6)
7th European Conference on Computational Fluid Dynamics (ECFD 7)
1115 June 2018, Glasgow, UK

NUMERICAL SIMULATION OF NONCLASSICAL AILERON BUZZ OVER 3D UNSTRUCTURED ADAPTIVE MESHES

Luca Cirrottola[1]*, Giuseppe Quaranta[1], Barbara Re[1a], Cécile Dobrzynski[2,3] and Alberto Guardone[1]

[1] Politecnico di Milano, Via La Masa 34, 20156 Milano (Italy)

[2] Inria Bordeaux Sud-Ouest, Team CARDAMOM, F-33405 Talence, France

[3] Bordeaux INP, IMB, UMR 5251, F-33400, Talence, France

*luca.cirrottola@polimi.it

Key words: Nonclassical aileron buzz, Computational aeroelasticity, Conservative mesh adaptation, Arbitrary Lagrangian–Eulerian formulation, Transonic flows

Abstract. Aileron buzz refers to the self–sustained oscillations of an aileron flapping behind an aircraft wing. Nonclassical buzz occurs in transonic flow regimes, and it is characterized by the oscillation of the shock wave location on and off the aileron surface. In order to simulate this phenomenon, we couple the rigid aileron dynamics with the finite volume ALE compressible flow solver Flowmesh. Dynamic grid adaptation is performed through the MMG remeshing library; a local conservative procedure tracks each mesh modification in time, thus avoiding any explicit solution interpolation step, while complying with the moving boundaries and performing solution–driven adaptation. We simulate a simplified test case, consisting of a straight wing between two walls, with a finite–span aileron. Simulations of different aileron spans highlight the 3D flow effects on the frequency of the aileron oscillations. Simulations over an alternative 2D setup, in which the aileron is still connected to the main wing by means of two flexible elements, show the influence of the air gap between aileron and wing on the shock wave movement and on the development of self–sustained aileron oscillations.

1 INTRODUCTION

Control–surface buzz is a class of phenomena characterized by self–sustained oscillations of a control surface on an aircraft wing, typically an aileiron flapping behind an aircraft wing in a transonic flow regime [1]. As explained in a 1962 report by Lambourne [1], this phenomenon was firstly observed in high subsonic flight in 1945 on a P-80 jet aircraft [1, 2] and then investigated by wind tunnel tests [3, 4] which showed

[a] *Present address*: Institute of Mathematics, University of Zürich, 8057 Zürich, Switzerland.

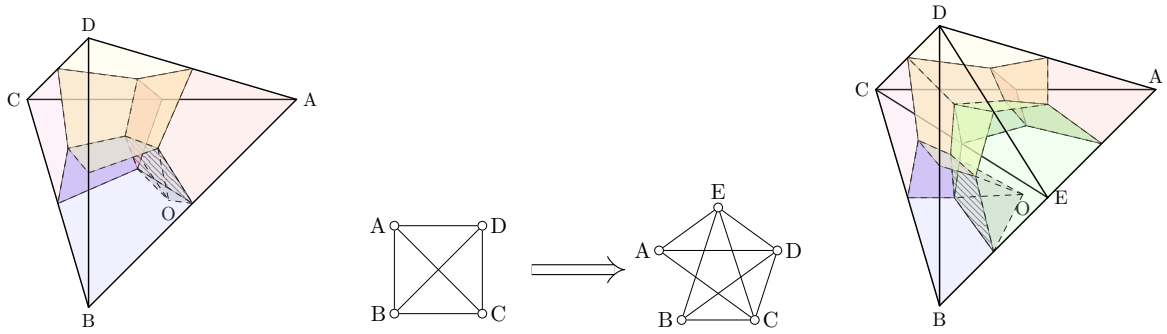

(a) Collapse to point O. (b) Connectivity change. (c) Expansion.

Figure 1: Example of three–steps conservative procedure for swept–volumes computation with connectivity change: Edge split.

that the phenomenon can be successfully reproduced by means of a single degree–of–freedom system (a freely–rotating aileron about its hinge) and that it is associated with the backwards and forwards movement of shock waves on the wing surface (and possibly the aileron surface) occurring with a phase lag with respect to the aileron oscillation. The extent of the local supersonic regions varies as the Mach number is increased, and allows to distinguish three main categories of buzz (type A, type B, type C) which are experienced with increasing flight speed [1]. Bendiksen [2] successfully reproduced the last two families of buzz, characterized by shock waves in proximity of the aileron hinge (type B) or the aileron trailing edge (type C), by means of inviscid flow calculations, and labeled them as *nonclassical* in order to stress the fact that they are not determined by shock–boundary layer interaction, differently from *classical* (type A) buzz which instead is determined by shock–induced separation. For nonclassical type B buzz, the onset of the instability appears to be determined by the oscillation in the shock wave location, while shock–induced flow separation influences the phenomenon by slowing down and stopping the aft movement of the shock wave.

Following several studies reported in [5, 3], we aim at studying the nonclassical type B aileron buzz with a model of a P–80 aircraft wing. Limit cycle oscillations are reported for this configuration at $M = 0.83$. We perform:

- *Three–dimensional simulations* for different aileron spans, in order to provide an assessment of three–dimensional effects.
- *Two–dimensional simulations* with and without wing–aileron air gap, in order to provide a first assessment of the effects of geometrical modeling.

2 NUMERICAL METHOD

We solve the Euler equations for inviscid compressible flows on unstructured simplicial meshes by means of the second order, total variation–diminishing, edge–based finite

volume solver `Flowmesh` [6, 7]. It couples an Arbitrary Lagrangian–Eulerian (ALE) formulation on dual median cells with dynamic mesh adaptation through the `MMG` remeshing library [8]. Time integration is performed through Backwards Difference Formulæ. A local conservative solution transfer procedure is employed at each time step [6, 7], so that the volumes swept by each dual cell interface during a mesh modification operation (edge split, edge collapse, barycentric node insertion, Delauney node insertion) can be computed and used to calculate mesh interface velocities needed in the ALE flux formulation, while automatically fulfilling a Discrete Geometric Conservation Law (DGCL) [9]. Figure 1 shows an example for an edge split operation. For each mesh element sharing the edge to be split, a three–steps procedure is adopted. Firstly, the whole element is collapsed to an arbitrary point O, and swept volumes are computed (fig. 1a). Then the mesh connectivity is changed, at time fixed (fig. 1b). Lastly, the new configuration is expanded to the current node positions, and swept volumes are computed again (fig. 1c).

2.1 Predictor–corrector coupled time integration of fluid flow and rigid control–surface dynamics

We consider a rigid control–surface, whose single degree of freedom is the rotation β about its hinge. The motion can be than computed by means of rigid body dynamics

$$\hat{J}\frac{\mathrm{d}^2\beta}{\mathrm{d}\tau^2} + \hat{C}\frac{\mathrm{d}\beta}{\mathrm{d}\tau} + \hat{K}\beta = C_M^f \tag{1}$$

where $\hat{J}$, $\hat{C}$, $\hat{K}$ are, respectively, the nondimensional rotational inertia, damping and stiffness, C_M^f is the aerodynamic moment coefficient of the control–surface (aileron, flap) about its hinge axis, and τ is the nondimensional time. A first–order system of equations in descriptor form [10] is obtained by defining the state vector and the system matrices and forcing

$$\mathbf{x} \triangleq \begin{bmatrix} \beta \\ \frac{\mathrm{d}\beta}{\mathrm{d}\tau} \end{bmatrix}, \qquad \mathbf{E} \triangleq \begin{bmatrix} 1 & 0 \\ 0 & \hat{J} \end{bmatrix}, \qquad \mathbf{A} \triangleq \begin{bmatrix} 0 & 1 \\ -\hat{K} & -\hat{C} \end{bmatrix}, \qquad \mathbf{f} \triangleq \begin{bmatrix} 0 \\ C_M^f \end{bmatrix} \tag{2}$$

so that the system reads

$$\mathbf{E}\frac{\mathrm{d}\mathbf{x}}{\mathrm{d}\tau} = \mathbf{A}\mathbf{x} + \mathbf{f} \tag{3}$$

At each time step, the aerodynamic forcing in system of equations 3 depends on the fluid flow around the control–surface at angle β. A coupled time integration procedure is thus needed for the fluid flow and control–surface dynamics. A convenient staggered solution of the fluid flow and control–surface motion can be achieved through the adoption of a predictor–corrector scheme. We use the predictor–corrector scheme proposed by Giles [11]

$$\begin{aligned}
&\text{Predictor:} && \left(\mathbf{E} - \frac{\Delta\tau}{2}\mathbf{A}\right)\mathbf{x}^* = \left(\mathbf{E} + \frac{\Delta\tau}{2}\mathbf{A}\right)\mathbf{x}^{(n)} + \Delta\tau\mathbf{f}^{(n)} \\
&\text{Evaluation:} && \mathbf{f}^* = \mathcal{F}(\mathbf{x}^*) \\
&\text{Corrector:} && \mathbf{E}\mathbf{x}^{(n+1)} = \mathbf{E}\mathbf{x}^{(n)} + \frac{\Delta\tau}{2}\mathbf{A}\left(\mathbf{x}^{(n)} + \mathbf{x}^*\right) + \frac{\Delta\tau}{2}\left(\mathbf{f}^{(n)} + \mathbf{f}^*\right)
\end{aligned} \tag{4}$$

At each time step, the predicted control–surface state $\mathbf{x}^*$ is used as a boundary condition for mesh deformation. When the mesh deformation becomes difficult, the time step is split in a sequence of K smaller steps $\delta\tau_k, k = 1, \dots, K$ in order to ease mesh deformation. In this case, multiple predictor steps have to be performed as follows

$$\begin{aligned} \mathbf{x}_0^* &= \mathbf{x}^{(n)} \\ \left(\mathbf{E} - \frac{\Delta\tau_k}{2}\mathbf{A}\right)\mathbf{x}_{k+1}^* &= \left(\mathbf{E} + \frac{\Delta\tau_k}{2}\mathbf{A}\right)\mathbf{x}_k^* + \Delta\tau_k \mathbf{f}^{(n)}, \qquad k = 0, \dots, K-1 \end{aligned} \tag{5}$$

Correction is performed only at the end of the time step, when it is actually possible to evaluate the current aerodynamic loads $\mathcal{F}(\mathbf{x}^*)$.

2.2 Nonlinear shape interpolation

Wing–flap configurations are mostly studied as two different rigid or elastic bodies, separated by a thin air gap. We would like to explore the effect of the air gap on shock wave motion and on aeroelastic stability by removing it and replacing it with a continuous surface connection. Modeling this connecting surface during an unsteady simulation with relative motion between airfoil and flap creates the necessity of parameterizing the surface motion so that it always remains attached to the moving bodies, while keeping a desired level of smoothness. We typically know an initial position of the surface $\mathbf{x}^{(0)} \in \mathbb{R}^d$, and possibly some other intermediate configurations or the final one $\mathbf{x}^{(T)} \in \mathbb{R}^d$. Since a detailed elastic model of the bodies is out of the scope of this work, we formulate our trajectory problem as a *shape morphing* problem, which is common to other research fields such as industrial design [12] and computer graphics [13, 14, 15].

For the present two–dimensional application, introducing a geometrical model of the initial and target configurations and directly interpolating in time the geometric model coefficients offers the possibility of preserving any desired curve smoothness along time. A possible boundary geometry model for the two–dimensional initial and target configurations $\mathbf{x}^{(0)}(\xi)$, $\mathbf{x}^{(T)}(\xi)$, parameterized on the reference domain $\xi \in [0, 1]$, and for the unknown shape $\mathbf{x}(\xi, t)$ in the interval $t \in [0, T]$ is given by a composite cubic Bézier approximation

$$\mathbf{x}^{(0)}(\xi) = \sum_{i=1}^{N-1} \mathbf{K}_i^{(0)} \mathbf{b}_i(\xi), \qquad \mathbf{x}^{(T)}(\xi) = \sum_{i=1}^{N-1} \mathbf{K}_i^{(T)} \mathbf{b}_i(\xi), \qquad \mathbf{x}(\xi, t) = \sum_{i=1}^{N-1} \mathbf{K}_i(t) \mathbf{b}_i(\xi) \tag{6}$$

We use an interpolation formula for the unknown discretized shape

$$\mathbf{K}_i(t) = \mathbf{F}(t)\mathbf{K}_i^{(0)} + \mathbf{G}(t)\mathbf{K}_i^{(T)}, \qquad i = 1, \dots, N-1, \quad t \in [0, T] \tag{7}$$

which is directly expressed in terms of the geometric model coefficients $\mathbf{K}_i(t)$. One possible way to choose an explicit expression of $\mathbf{F}(t)$ and $\mathbf{G}(t)$ is to comply with the flap rotation $\Delta\mathbf{R}\left(\beta(t)\right)$ relative to the initial configuration. Its initial value is thus $\Delta\mathbf{R}(\beta(0)) = \mathbf{I}$, while the target one $\Delta\mathbf{R}(\beta(T)) = \Delta\mathbf{R}^{(T)}$ depends from the choice of the target configuration.

Imposing the compatibility of flap rotation with shape morphing in the connection point gives the expression of the interpolation matrices

$$\begin{aligned} \mathbf{G}(t) &\triangleq \left(\mathbf{I} - \Delta\mathbf{R}\left(\beta(t)\right)\right)\left(\mathbf{I} - \Delta\mathbf{R}^{(T)}\right)^{-1} \\ \mathbf{F}(t) &\triangleq \Delta\mathbf{R}\left(\beta(t)\right) - \mathbf{G}(t)\Delta\mathbf{R}^{(T)} \end{aligned} \tag{8}$$

It can be verified that this choice automatically fulfills the interpolation conditions

$$\begin{aligned} \mathbf{F}(0) &= \mathbf{I}, \qquad \mathbf{F}(T) = \mathbf{0} \\ \mathbf{G}(0) &= \mathbf{0}, \qquad \mathbf{G}(T) = \mathbf{I} \end{aligned} \tag{9}$$

It should be noted that, although the present interpolation of the geometrical model guarantees C^2 continuity $\forall \xi \in (0,1)$, the current choice of the interpolation matrices only preserves C^0 smoothness at end points. This issue is in fact shared by other shape morphing models considered for this work.

Flawless interaction of the nonlinear shape interpolation procedure with dynamic mesh adaptation relies on the distinction of curve *control points* from *evaluation points*. Curve *knots/control points* are not boundary grid points. Having defined the same composite cubic Bézier model for all the curve shapes in the time interval $t \in [0, T]$ means that the number of spline control points remains constant in time. Boundary mesh points are *evaluation points* of the geometric model. Each time that mesh adaptation inserts a new node on the boundary, its parametric coordinate ξ is guessed from the average of the parametric coordinates of its neighbors (or it is set from the solution of the curve equation through bisection/Newton method, not needed in this work), then the position is corrected by evaluating the geometrical model at ξ.

3 GEOMETRICAL SETUP

We start from the same case studied in [5], with a NACA$65_1$213($a = 0.5$) airfoil wing in a $M = 0.83$ flow. Due to the low tapering of the wing, we simplify the analysis by considering a straight wing enclosed between two wind tunnel walls. The slip boundary condition in an inviscid compressible flow model is equivalent to imposing a symmetry condition on side walls.

Three–dimensional model. Figure 2 shows the separate geometrical models for three–dimensional wing and aileron, made with the GMSH software [16]. The wing has a nondimensional chord length $c = 1$, and total span $L = 1.5$. The aileron hinge axis is set at a horizontal distance $x_h = 0.75$ from the wing leading edge. The vertical position of the aileron hinge is chosen so that it is at the same vertical distance from the upper and lower surface, thus $y_h = 0.00854$ above the line connecting leading and trailing edge. In this way, the aileron front surface is made from a circular arc with center in the aileron hinge axis. Since its connection with the upper and lower surface is sharp, a fillet operation is used to smoothen both the connections. The aileron cut inside the wing is created according to the same procedure, starting with a circular cut centered in the hinge axis,

with an additional gap of width $g = 0.01$ between wing and aileron. The side cut allows for an aileron span $b = 1.0$ and is realized with the same gap width $g = 0.01$. Figure 3 shows the initial mesh for the compound wing–aileron configuration.

Two–dimensional model. For two–dimensional analyses over a discontinuous wing–aileron configuration, with an air gap between the two solid bodies, the same cutting procedure used for the 3D model is employed (fig. 4a, 4b). In order to study also a continuous wing–aileron configuration, without air gap between the two solid bodies, two regions on the upper and lower airfoil surface are identified (orange and cyan lines in fig. 4c, 4d), in order to move these strips in time according to the shape interpolation procedure described in section 2.2, driven by the aileron angle $\beta(t)$.

4 RESULTS

In this section, the numerical methodology proposed in section 2 is applied to the free rotation of a three–dimensional aileron with null stiffness and damping. The equation is coupled with the flow solver through the predictor–corrector procedure described in section 2.1. Following reference [17] the aileron has inertia per unit span $\tilde{J} = 0.24217$ kg m. The nondimensional inertia $\hat{J}$, in three–dimensions, is found as

$$\hat{J} = \frac{\tilde{J}b}{q_\infty c^3 \mathcal{T}^2} \tag{10}$$

where $q_\infty = 31097$ Pa, and the time constant $\mathcal{T} = 0.00544$ s is set from the dimensional chord $c = 1.472$ m and the flight speed $V_\infty = 270.5$m/s.

4.1 Validation

Validation of aerodynamic loads is performed by comparing the computed pressure loads with the experimental data for the NACA$65_1$213 ($a = 0.5$) airfoil available in [18].

Prior to simulating the physical system in a dynamically instable condition, we verify the numerical stability of the coupled predictor–corrector scheme by coupling the fluid flow equations with a mass–spring aileron nondimensional equation of motion

$$\hat{J}\frac{\mathrm{d}^2\beta}{\mathrm{d}\tau^2} + \hat{K}\beta = 0 \tag{11}$$

with initial conditions $\beta(\tau = 0) = 0$ and $\frac{\mathrm{d}\beta}{\mathrm{d}\tau}(\tau = 0) = \kappa B$. This allows us to reproduce a harmonic response $\beta(\tau) = B\sin(\kappa\tau)$ with user–defined reduced frequency $\kappa = (\hat{K}/\hat{J})^{1/2}$ and amplitude B.

This test condition is used to analyze the effects of different mesh refinement levels during the time simulation. Figure 5 shows lift and moment coefficient histories for a harmonic response test at $\kappa = 0.75398$ with amplitude $B = 10°$ for mesh refinement levels which keep the number of mesh nodes between 180000 and 240000 (labeled as *base*), between 230000 and 290000 (*medium*), and between 280000 and 320000 (*fine*).

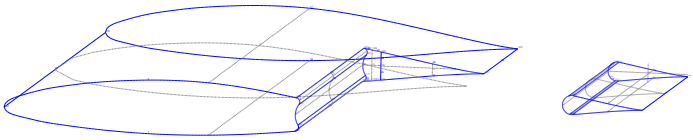

(a) Wing. (b) Aileron.

Figure 2: Three–dimensional geometrical model.

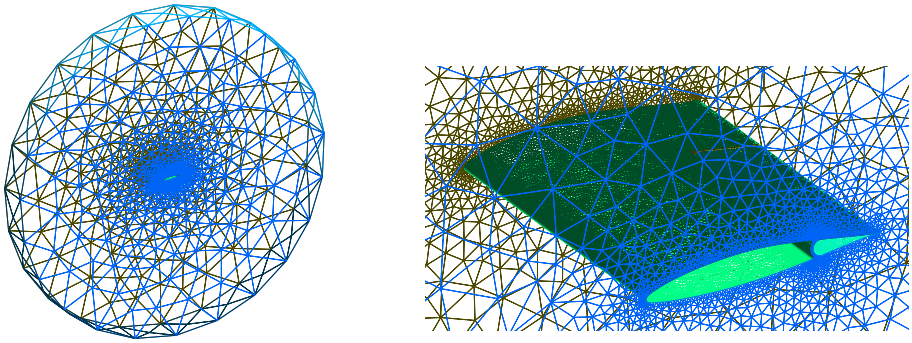

Figure 3: Three–dimensional initial mesh, with zoom (93729 domain nodes and 528921 elements, minimum edge size $h_{\min} = 0.0015$).

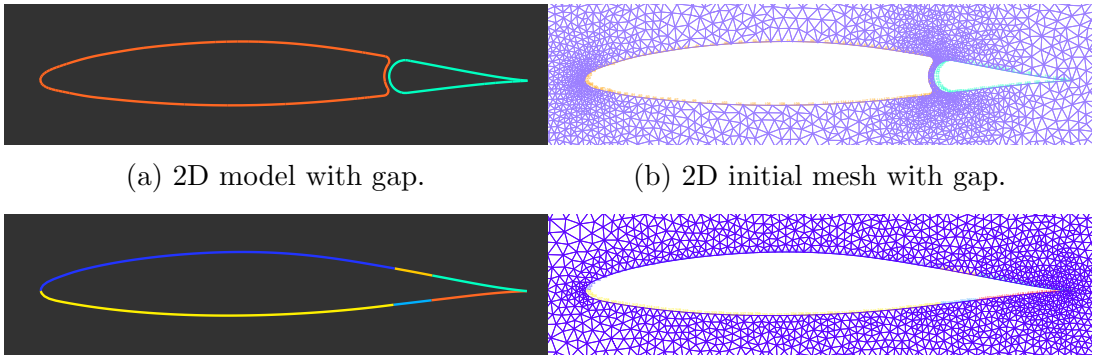

(a) 2D model with gap. (b) 2D initial mesh with gap.

(c) 2D model without gap. (d) 2D initial mesh without gap.

Figure 4: Two–dimensional geometrical model and initial mesh, with and without gap between wing and aileron.

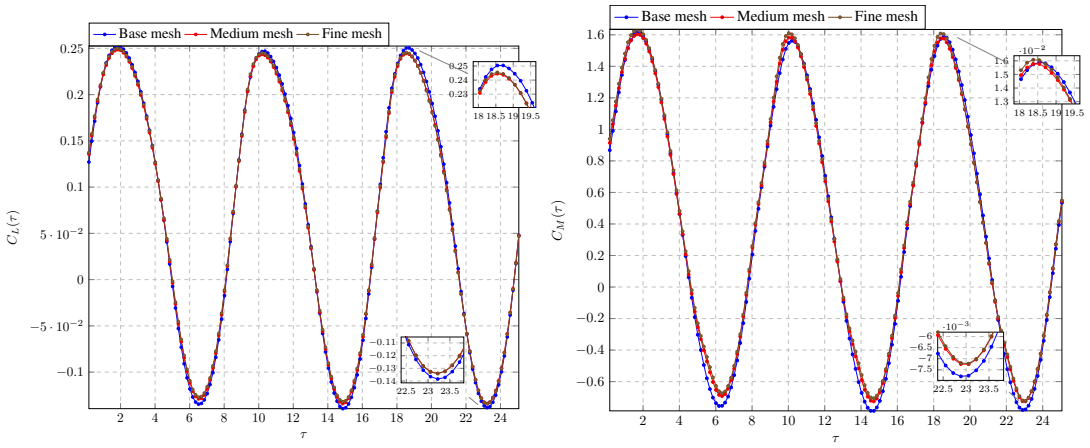

(a) Lift coefficient time history.

(b) Moment coefficient time history.

Figure 5: Lift and moment coefficient for a test harmonic response at $\kappa = 0.75398$ with amplitude $B = 10°$.

Finally, dimensional frequencies $f = (\kappa V_\infty)/(2\pi c)$ computed in the buzz study reported in the next section for several aileron span and for Mach number between $M = 0.83$ and $M = 0.85$ are in the range between 16.7 Hz and 21.7 Hz, in good accordance with flight tests [18] and wind tunnel data [3] which report a frequency range between 19.4 and 28 Hz.

4.2 Three–dimensional buzz simulations, varying finite aileron span

We investigate the frequency trend as the finite aileron span is changed. We test four configurations, for progressively shorter aileron spans $b = 1, 0.75, 0.5, 0.25$. Aileron inertia is scaled accordingly. The span of the wing root is kept fixed. Moment coefficient and aileron angle results (fig. 6) show that the amplitude of the moment coefficient oscillations is progressively smaller, consistently with the reduced size of the aerodynamic surface, while aileron angle oscillations exhibit a quicker converge to a limit cycle solution. Oscillation frequencies decrease as the aileron span is reduced.

Analysis of shock waves motion (fig. 7) shows that the effect of the spanwise air gap between wing and aileron is that of imposing an abroupt flow deceleration at the end of the wind surface through a first shock wave, with a new acceleration of the flow on the aileron surface causing a second shock wave to appear during sufficiently wide upstroke or downstroke aileron motions. This re–acceleration is not possible inside the chordwise wing–aileron air gap, so the aileron shock wave always starts from the aileron front corner and follows a curved pattern on the aileron surface, where the flow acceleration is stronger. This curved shock pattern influences aileron pressure load as its span is varied, providing an explaination for the variation in the oscillation frequency and amplitude.

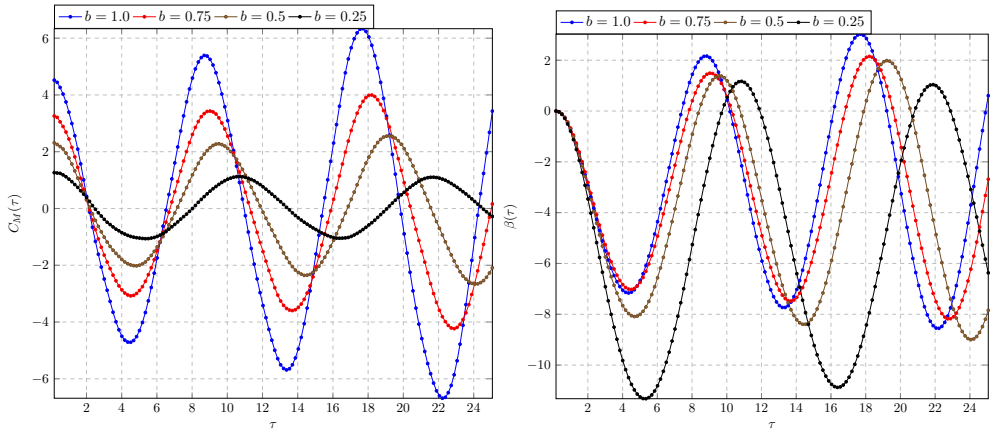

(a) Moment coefficient time history. (b) Aileron angle time history.

Figure 6: Moment coefficient and aileron angle history with varying aileron span.

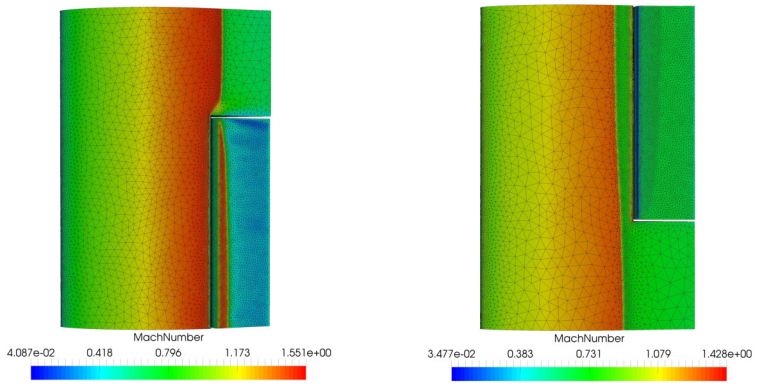

(a) Downstroke (top view). (b) Downstroke (bottom view).

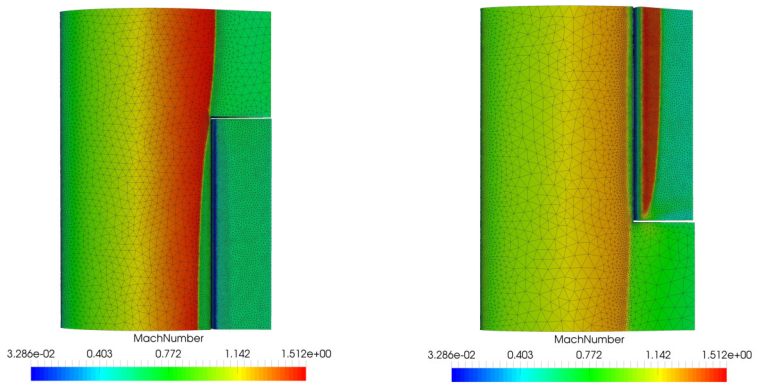

(c) Upstroke (top view). (d) Upstroke (bottom view).

Figure 7: Mach number distribution on wing surface, wing span $L = 1.5$, aileron span $b = 1.0$. Downstroke motion at $\beta = 4.24°$, upstroke motion at $\beta = -10.12°$. Left: Top view. Right: Bottom view.

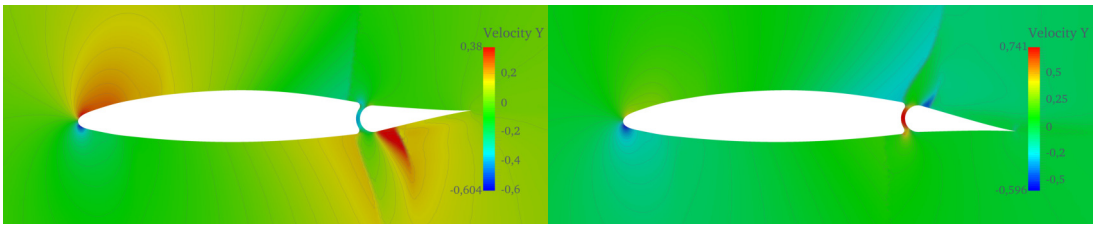

(a) Upstroke, $\beta = -7.02°$. (b) Downstroke, $\beta = 5.73°$.

Figure 8: Vertical velocity at $M = 0.83$ for the discontinuous wing–aileron configuration, in a peak aft movement of the lower and upper shock.

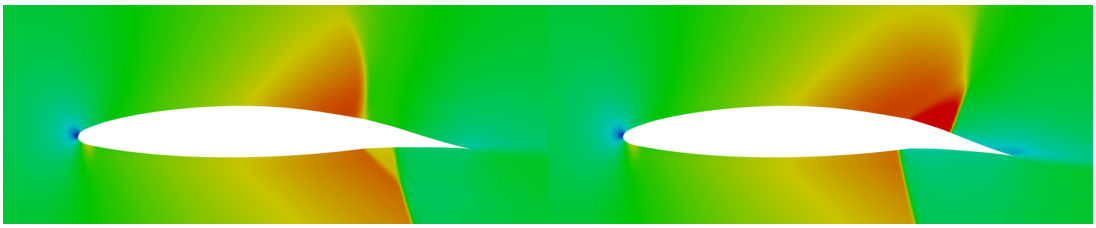

(a) Upstroke, $\beta = 6.66°$. (b) Downstroke, $\beta = 10.52°$.

Figure 9: Mach number at $M = 0.84$ for the continuous wing–aileron configuration (starting with $\beta_0 = -6°$), in a peak aft movement of the lower and upper shock.

4.3 Two–dimensional simulations over discontinuous and continuous wing–flap configurations

In this section, we compare the discontinuous and continuous wing–aileron configurations (with and without air gap) shown in fig. 4. Without gap, a stable fixed point configuration is found at $M = 0.83$, differently to the discontinuous configuration at the same Mach number.

The difference in the aileron behavior for the two geometrical configurations can be appreciated by analyzing the flow field. In the discontinuous configuration, the curvature of the gap corners on the back of the wing imposes an abrupt deceleration of the flow in the downstream direction, making each corner an upper limit for the aft movement of shock waves. If the flow accelerates again downstream beyond these points, new shocks will form on the surface of the aileron. The flow inside the gap appears to change in direction between upstroke and downstroke aileron motions (fig. 8), in phase with the formation of new shocks on the lower or upper surface of the aileron. This mechanism appears to take place in each buzz condition with discontinuous bodies, both in 2D and in 3D.

On the other hand, in the continuous configuration the initial shock location is already different from the one over the discontinuous configuration, suggesting that the buzz boundary could be different [2]. In fact, starting from an initial condition $\beta_0 = 0°$, in the current analysis buzz oscillations are found again at $M = 0.85$. Buzz oscillations

can be found for a lower Mach number if the initial condition is changed, as it is the case when $\beta_0 = -6°$ at $M = 0.84$. In this configuration, there is no flow leakage or structural discontinuity impeding shock waves from traveling all over the upper or lower surface, but changes in surface curvature play a role in modifying the shock pattern. Since the nonlinear shape interpolation procedure presented in section 2.2 is sufficient to get an analytical expression for the surface movement with arbitrary degree of continuity, while preserving only C^0 continuity at the end points (a problem shared by other PDE–based interpolation methods), the end points act as triggers for an expansion fan (during downstoke movements) or a shock (during upstroke movements) upstream of the already present shock traveling on the aileron surface. This results, respectively, in the delta shock pattern and the expansion fan–shock interaction showed in fig. 9.

5 CONCLUSIONS

We have studied a fluid—structure interaction method for rigid body dynamics in inviscid compressible flows, over body–fitted adaptive meshes. We have coupled the predictor–corrector time integration scheme proposed in [11] with the ALE formulation proposed in [6, 7] for local conservative mesh adaptation. In order to analyze the effects of the structural discontinuity between wing and aileron on system dynamics, a nonlinear shape interpolation procedure for the time evolution of continuous wing–aileron configurations is developed.

This methodology is employed to the simulation of nonclassical aileron buzz [1, 2] over a straight NACA$65_1$213 ($a = 0.5$) wing setup. Mesh adaptation allows to preserve the validity and quality of the body–fitted mesh with large relative body motions. We have shown three–dimensional simulations for varying aileron spans, and we have compared two–dimensional simulations with and without structural continuity between wing and aileron. Results show that the chordwise wing–aileron air gap influences oscillations by constraining shock waves on the aileron surface to start from its corner and to form a curved pattern that influences the flap aerodynamic moment, while the spanwise wing–aileron air gap imposes a sudden flow deceleration that stops the downstream motion of shock waves, allowing for the formation of a second shock wave further downstream on the surface of the aileron.

The current computational procedure can be further applied to the aeronautical study of different discontinuous wing–aileron geometrical configurations, as well as it can be extended with the inclusion of a fluid–structure interface scheme in order to perform aeroelastic simulations with elastic bodies.

References

[1] N. C. Lambourne. *Control–surface buzz*. Aeronautical Research Council Reports and Memoranda, 1962.

[2] Oddvar O. Bendiksen. “Nonclassical aileron buzz in transonic flow”. In: *Structures, Structural Dynamics, and Materials and Co-located Conferences*. American Institute of Aeronautics and Astronautics, Apr. 1993.

[3] Albert L. Erickson and Jack D. Stephenson. *A Suggested Method of Analyzing for Transonic Flutter of Control Surfaces Based on Available Experimental Evidence*. National Advisory Committee for Aeronautics, 1947.

[4] Albert L Erickson and Robert L Mannes. *Wind-Tunnel Investigation of Transonic Aileron Flutter*. National Advisory Committee for Aeronautics, 1949.

[5] A. Carbonara. "Sviluppo di modelli aerodinamici di ordine ridotto per l'analisi del buzz di alettone". Politecnico di Milano, 2016.

[6] D. Isola, A. Guardone, and G. Quaranta. "Finite-volume solution of two-dimensional compressible flows over dynamic adaptive grids". In: *Journal of Computational Physics* 285 (2015), pp. 1 –23.

[7] B. Re, C. Dobrzynski, and A. Guardone. "An interpolation-free ALE scheme for unsteady inviscid flows computations with large boundary displacements over three-dimensional adaptive grids". In: *Journal of Computational Physics* 340 (2017), pp. 26 –54.

[8] C. Dapogny, C. Dobrzynski, and P. Frey. "Three-dimensional adaptive domain remeshing, implicit domain meshing, and applications to free and moving boundary problems". In: *Journal of Computational Physics* 262 (2014), pp. 358 –378.

[9] S. Étienne, A. Garon, and D. Pelletier. "Perspective on the geometric conservation law and finite element methods for ALE simulations of incompressible flow". In: *Journal of Computational Physics* 228.7 (2009), pp. 2313 –2333.

[10] Guang-Ren Duan. *Analysis and design of descriptor linear systems*. Vol. 23. Springer Science & Business Media, 2010.

[11] M.B. Giles. "Stability Analysis of a Galerkin/Runge–Kutta Navier–Stokes Discretisation on Unstructured Tetrahedral Grids". In: *Journal of Computational Physics* 132.2 (1997), pp. 201 –214.

[12] S. E. Chen and R. E. Parent. "Shape averaging and its applications to industrial design". In: *IEEE Computer Graphics and Applications* 9.1 (1989), pp. 47–54.

[13] Francis Lazarus and Anne Verroust. "Three-dimensional metamorphosis: a survey". In: *The Visual Computer* 14.8 (1998), pp. 373–389.

[14] Marc Alexa. "Recent advances in mesh morphing". In: *Computer graphics forum*. Vol. 21. 2. Wiley Online Library. 2002, pp. 173–198.

[15] Dong Xu et al. "Poisson shape interpolation". In: *Graphical Models* 68.3 (2006). SPM 2005, pp. 268 –281.

[16] Christophe Geuzaine and Jean-François Remacle. "Gmsh: A 3-D finite element mesh generator with built-in pre-and post-processing facilities". In: *International journal for numerical methods in engineering* 79.11 (2009), pp. 1309–1331.

[17] James T. Howlett. *Calculation of unsteady transonic flows with mild separation by viscous-inviscid interaction*. NASA Technical Paper. NASA Langley Research Center, 1992.

[18] Harvey H. Brown, Jr. Rathert George A., and Lawrence A. Clousing. *Flight-test measurements of aileron control surface behavior at super critical Mach numbers*. NACA Research Memorandum A7A15. Ames Aeronautical Laboratory, 1947.